



1 **Study on the influence of topography on wind shear-**
2 **numerical simulation based on WRF-CALMET**

3 Xingyu Wang, Yuhong Lei, Baolong Shi, Zhiyi Wang, Xu Li, Jinyan Wang, Key
4 Laboratory of Climate Resource Development and Disaster Prevention in Gansu
5 Province, College of Atmospheric Sciences, Lanzhou University, Lanzhou 730000,
6 China

7 E-mail:u220220903271@lzu.edu.cn

8 **Abstract**

9 This study focuses on the critical issue of low-altitude wind shear, vital for
10 aircraft safety during takeoff and landing. Using the WRF-CALMET model, we assess
11 the impact of topography on low-level wind shear at Zhongchuan Airport. CALMET
12 outperforms WRF, showing improved simulation accuracy. CALMET's simulation
13 highlights diurnal variations in vertical wind shear, especially pronounced from
14 13:00 to 24:00. Notably, CALMET indicates 1-2 hazard levels higher wind shear for
15 aircraft operations compared to WRF in a significant area. Terrain sensitivity
16 experiments reveal CALMET's responsiveness to terrain changes during high wind
17 shear periods, with reduced impact at higher altitudes. CALMET's incorporation of
18 kinematic terrain influences, blocking effects, slope flow, and strengthened
19 diversion of near-surface airflow on complex terrain contribute to these
20 findings. This study confirms the efficacy of CALMET in simulating low-altitude wind
21 shear, emphasizing its superiority in capturing terrain influences and reducing the
22 aviation safety threat posed by low-altitude wind shear.

23 **Keywords** — wind shear; wind field-numerical simulation; airport; CALMET;
24 aeronautical meteorology; topographic effect

25 **1. Introduction**

26 According to the definition of the International Civil Aviation Organization
27 (ICAO), low-level windshear refers to the sharp change of spatial wind speed or
28 direction within a 600-meter altitude range. Wind shear includes both vertical and
29 horizontal components and typically occurs near fronts, coastlines and the surface.
30 In the process of taking off and landing, low-level wind shear will affect the airspeed
31 of the aircraft, causing great risks and even terrible accidents in serious cases
32 (Evans J, 1989). In June 1975, a Boeing 727 aircraft crashed during its landing at
33 Kennedy Airport due to encountering low-level wind shear, resulting in 113
34 fatalities and 11 injuries (Fujita T T, 1997); In June 2000, a Wuhan Airlines aircraft
35 crashed during landing, also due to encountering low-level wind shear. In 2017, a



36 New Zealand Airlines A320-200 aircraft experienced low-level wind shear during
37 landing, resulting in severe damage to the aircraft and significant economic losses.
38 Therefore, accurate simulation and prediction of low-level wind shear, especially on
39 complex terrain, is of great significance for ensuring the safety of aircraft takeoffs
40 and landings at airports.

41 However, achieving accurate predictions remains a primary challenge faced by
42 numerical weather forecasting models (Colman B.2012). Low-level wind shear is
43 influenced by multiscale weather systems and characterized by small temporal and
44 spatial scales, high intensity, and sudden occurrences, thus making it difficult to
45 detect, study and predict. The numerical weather forecast (NWP) model with 200-
46 meter resolution was used to forecast low-level wind shear at Hong Kong
47 International Airport. During the whole research period, the results consistent with
48 the model forecast were observed on both runways(Hon K K.2020). The Weather
49 Research and Forecasting (WRF) model, designed for high-resolution mesoscale
50 weather forecasting, simulates airflow under realistic atmospheric conditions.
51 However, due to the grid resolution of WRF being greater than 1 km, it struggles to
52 simulate the small-scale airflow movements in complex terrain. Hong Kong
53 International Airport previously attempted to predict wind shear using the WRF
54 model, affirming its capability to forecast wind shear induced by terrain changes
55 several hours in advance. However, providing precise warnings for the airport
56 proved challenging(Chan PW.2016). Since then, Hong Kong International Airport
57 has carried out improved research on wind shear simulation based on WRF, and
58 captured the characteristics of wind and micro-scale airflow in many airports by
59 WRF-LES (Chen F.2022)

60 Lanzhou Zhongchuan International Airport stands as one of the largest aviation
61 hubs in Northwest China, situated in the southeastern part of the Qinwangchuan
62 alluvial-fan basin, surrounded by mountains on all sides. The region is known for
63 frequent wind shear occurrences, a phenomenon that has become increasingly
64 common at Lanzhou Zhongchuan Airport due to the rapid growth in the number of
65 flights. Most wind shear events occur during spring and summer, particularly in May,
66 June, and July (Li L.2020). Statistical reports on wind shear at Lanzhou Zhongchuan
67 Airport indicate that the majority of incidents occur in the afternoon and evening.
68 This trend is attributed to the downward momentum in the afternoon, enhanced
69 convective activity from increased ground heating, and higher wind speeds. Severe
70 convective weather is more likely to occur in the late afternoon to evening,
71 contributing to a higher frequency of reported low-level wind shear events.
72 Conversely, fewer flights operate during the night, accompanied by reduced
73 convective weather, resulting in relatively fewer reports of aircraft encountering
74 low-level wind shear (Dang B.2013). In May 2016, Zhongchuan Airport installed
75 coherent Doppler lidar near the runway to study the characteristics of low-level
76 wind shear and provide warnings (Li L.2020). Numerical simulation studies on
77 wind shear at Zhongchuan Airport have been ongoing. Jiang L. et al. selected a 6
78 km×6 km area near the runway at Zhongchuan Airport to establish a digital
79 elevation model of the terrain. They used FLUENT software for numerical



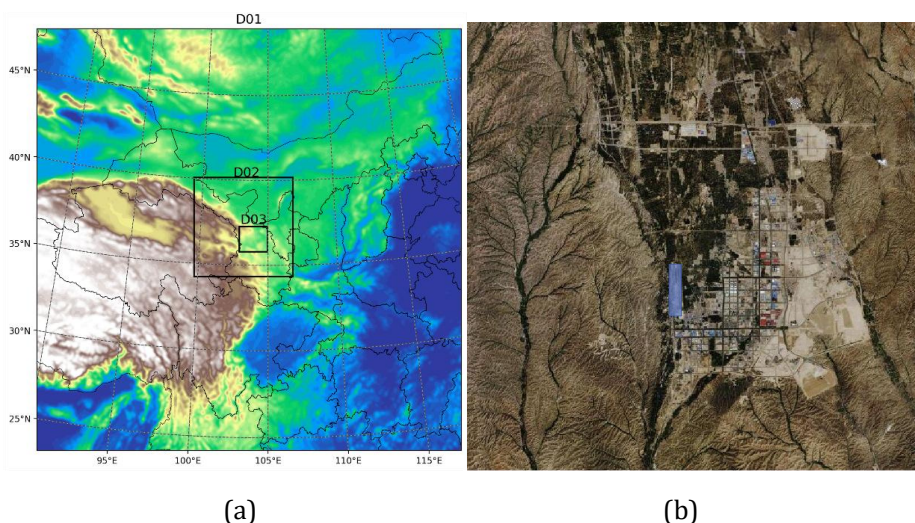
80 simulation, solving iterative calculations to obtain the distribution characteristics of
81 wind speed and pressure in the simulated area (Jiang Lihui.2018). However,
82 FLUENT, being a Computational Fluid Dynamics (CFD) simulation software widely
83 used in engineering, science, and research fields, only considers the local turbulence
84 of terrain and buildings on the flow field. It does not account for factors such as
85 gravity and heat exchange in real atmospheric conditions. Therefore, relying solely
86 on FLUENT for simulating and warning wind shear at Zhongchuan Airport has its
87 limitations. Improvements in simulating low-level wind shear still require
88 enhancements built upon numerical weather forecasting models.

89 In both domestic and international research, the CALMET model is frequently
90 employed to downscale WRF, providing a finer representation of microscale terrain
91 structures. Particularly in weak wind conditions, the CALMET downscaling coupling
92 model outperforms WRF in simulating near-surface wind directions(Zhang D.2020).
93 The WRF/CALMET coupled system demonstrates satisfactory performance in
94 various challenging scenarios, including the complex terrain of the Qinghai-Tibet
95 Plateau(Liao R.2021) and the intense weather system of Super Typhoon Meranti
96 (2016)(Tang S.2021). Up to now, no one has used WRF/CALMET coupling system to
97 simulate and test the occurrence of low-altitude wind shear. The aim of this study is
98 to leverage the CALMET model's dynamic downscaling effect on local micro-terrain,
99 providing an improved method for simulating low-level wind shear within the WRF
100 model.

101 **2.Mode, Data, Method and Experimental Setup**

102 2.1 Models and Experimental Setup

103 In this study, the WRF model (version 4.2) was employed to simulate a severe
104 convective weather event occurring in the vicinity of Zhongchuan Airport over a
105 duration of 96 hours, starting from July 2, 2022, at 0000 UTC. The simulated wind
106 field results were then downscaled to 100 meters through coupling with the
107 CALMET model. The model utilized a three-layer, two-way nested domain
108 configuration (Figure 1a), with horizontal grid spacings of 9 km, 3 km, and 1 km.
109 In the vertical direction, there were 39 complete Eta layers from the surface to 0 hPa.
110 The physical schemes employed by WRF are detailed in Table 1.



111

112

113

114

115

116

Figure 1. Three-layer Nested Domains of the WRF Model (a) and Simulation Area of the CALMET Model © Google Maps(b), with the Zhongchuan Airport Highlighted in Blue

Table 1. Model Configuration

Physical Scheme	WRF Option
Microphysics	Thompson graupel scheme (2-moment scheme in V3.1)
Cumulus parameterization	Tiedtke scheme
Longwave radiation	RRTMG
Shortwave radiation	RRTMG
Surface layer	Monin-Obukhov (Janjic Eta) scheme
Land surface	Noah
Boundary layer	MYJ

117

118

119

120

121

122

123

124

125

126

The diagnostic model utilized in this research is the CALMET model (version 6.5), which constitutes the meteorological component of the California Puff Dispersion Model (Scire J S.2000). In the configuration of this study, the initial guessed wind field is obtained from the grid wind field generated by the innermost domain of WRF, with a horizontal grid spacing of 1 km (D3 in Figure 1(a)). Since no objective analysis procedure is employed, we only pay attention to the first step wind field. The coverage area of the CALMET model encompasses Zhongchuan Airport and its surrounding 38km×38km region (Figure 1(b)), with a horizontal resolution of 100m. The vertical layers are set to 10 height levels within 600 m from the ground (the height range influenced by low-level wind shear).

127

128

Terrain Sensitivity Experiments for Demonstrating the Impact of Terrain on Wind Shear Simulation in CALMET:

129

130

(1) CALMET: CALMET model configured with default settings as described earlier.



131 (2) CALEMT_FLAT: Modification in the TERREL terrain processing module
132 where the elevation of all grid points is adjusted to 2000 meters. This adjustment
133 facilitates CALMET simulation on a flat underlying surface.

134 (3) CALEMT_RAISE: Modification in the TERREL terrain processing module
135 where the elevation of grid points with an altitude exceeding 2050 meters is
136 increased by 1.5 times. This modification enables CALMET to simulate wind shear
137 over a more rugged terrain.

138 These terrain sensitivity experiments are designed to showcase how variations
139 in terrain impact wind shear simulation within CALMET. The CALMET_FLAT
140 experiment simulates wind shear on a flat surface, while the CALMET_RAISE
141 experiment explores wind shear simulation over steeper terrain. The comparison of
142 results from these experiments with the default CALMET setting will provide
143 insights into the sensitivity of wind shear simulations to terrain variations.

144 2.2 data

145 The terrain data comes from the global 90 m digital elevation data set of Shuttle
146 Radar Topography (SRTM3 V4.1) of NASA, and the land use data comes from the
147 global land cover type data with 10m resolution of Pengcheng Laboratory
148 (<https://data-starcloud.pcl.ac.cn/zh>) of Tsinghua University in 2017.

149 The horizontal resolution of the ECMWF Reanalysis v5 (ERA5) dataset is $0.25^\circ \times$
150 0.25° , with a temporal resolution of 1 hour. This dataset is employed as both the
151 initial input and boundary fields for WRF model. Additionally, this study utilizes
152 ERA5 variables, specifically geopotential height and temperature, for analyzing
153 weather systems during periods of intense convection.

154 Observational data for ground-level 10m wind speed at Lanzhou Zhongchuan
155 Airport are sourced from historical wind speed records provided by the National
156 Oceanic and Atmospheric Administration (NOAA)
157 (<https://www.ncei.noaa.gov/maps/daily/>) with a temporal resolution of 1 hour.
158 The ground 10m wind speed data of WRF model, CALMET model and ERA5
159 reanalysis data are interpolated to the location of Zhongchuan Airport, and
160 compared with the observed data to verify the performance of the models.

161 2.3 method

162 To quantify the differences in 10m wind speed among the experiments, the
163 following statistical metrics are employed:

164 Index of agreement (IA):

$$165 \quad IA = 1 - \frac{\sum_{i=1}^N (P_i - O_i)^2}{\sum_{i=1}^N (|P_i - \bar{O}| + |O_i - \bar{O}|)^2} \quad (1)$$



166

167 Root-mean-squared error (RMSE):

$$168 \quad \text{RMSE} = \sqrt{\frac{1}{n} \sum_{i=1}^n (O_i - P_i)^2}. \quad (2)$$

169 Mean relative error (MRE):

$$170 \quad \text{MRE} = \frac{1}{n} \sum_{i=1}^n \frac{(P_i - O_i)}{O_i} \quad (3)$$

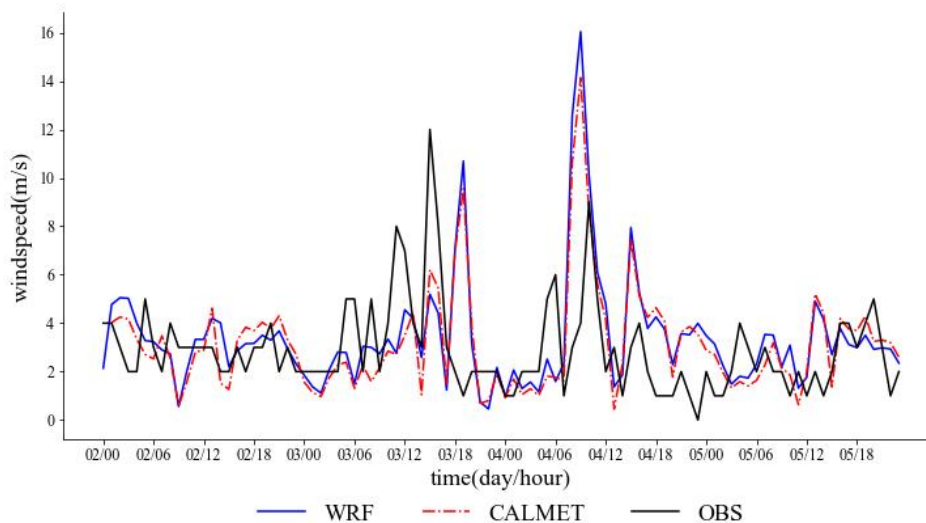
171 Here, \bar{O} and \bar{P} represent the average values of observational and simulated data,
172 respectively. Each observed value is denoted as O_i , and each simulated value is
173 denoted as P_i . Smaller values for MRE and RMSE, and an IA closer to 1.0, indicate
174 better simulation performance.

175 Wind shear can be categorized into three types: vertical shear β , meridional
176 horizontal shear α_1 , and zonal horizontal shear α_2 . Among these, vertical shear of
177 horizontal wind has a more significant impact on aircraft takeoff and landing
178 compared to the other types (Bretschneider, L.2022). It results in changes in wind
179 speed and direction as an aircraft moves through different altitudes, which can lead
180 to drastic changes in airflow during ascent or descent, thereby increasing flight
181 difficulty, particularly during takeoff and landing (Keohan, C.2007; Eggers, A.J.,
182 Jr.2003; Eggers, A.J., Jr.1992).

183 **3.Result**

184 3.1 Improvement of WRF/CALMET coupling model for simulation of low-level
185 wind shear.

186 We evaluated the performance of two models in simulating near-surface wind
187 speeds, as shown in Figure 2 and Table 2. Both models showed better agreement
188 with observed data during periods of low wind speeds before convective
189 development (06:00 on July 3) and after convective cessation (02:00 on July 5).
190 During periods of intense convection, both models captured wind speed variability.
191 Although both experiments underestimated or overestimated peak wind speeds on
192 July 3 and July 4, CALMET slightly outperformed WRF in simulating high wind
193 speeds. Furthermore, Table 2 indicates that CALMET's Mean Relative Error and
194 Root Mean Squared Error were lower than those of WRF throughout the entire
195 simulated period, with improvements of 11.13% and 7.24%, respectively. CALMET's
196 Index of Agreement was also closer to 1 compared to the WRF experiment, with an
197 improvement of 12.06%. These results demonstrate CALMET's superior overall
198 simulation performance compared to WRF.



199

Figure 2 :the time series of 10m surface wind speed for both numerical simulations and observational data

200

201

202

203

Table 2: Statistic results of near-surface wind speed simulations in different experiments averaged.

204

205

	WRF	CALMET	Improvement (%)
MRE (%)	43.255	38.425	11.13
RMSE(m/s)	2.713	2.517	7.24
IA	0.454	0.509	12.09

206

207

208

209

210

211

212

213

214

215

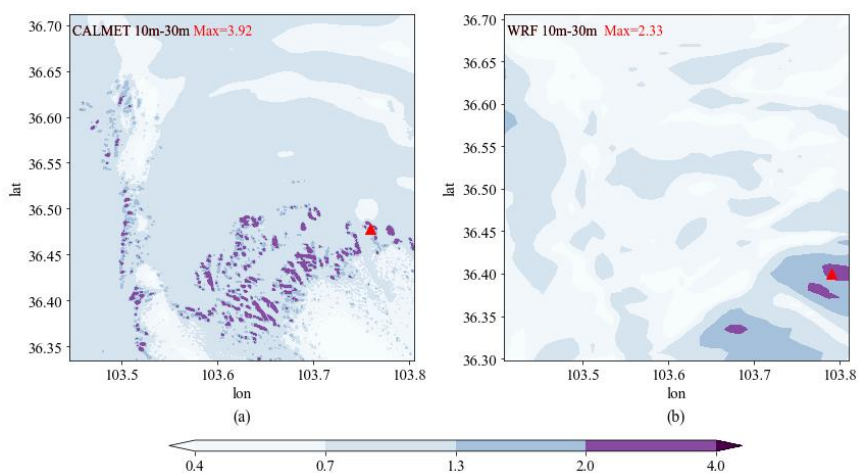
216

At 16:00 on July 3, significant fluctuations in surface wind speeds mark the onset of convective development (Figure 2). Figure 3 illustrates the distribution of Vertical Wind Shear (VWS) simulated by both models. In the layer between 10m and 30m above ground level, CALMET's maximum VWS values, while consistent in location with WRF's, are notably higher. Terrain analysis reveals CALMET simulates high VWS values near mountain foothills and western slopes (Figure 8). WRF's high VWS values primarily occur in mountainous regions. Details for the height layers of 200m-300m and 500m-600m can be found in the appendix. Overall, both models exhibit decreasing VWS with increasing height. From the overall distribution of VWS, CALMET can simulate a wider range of third and fourth level wind shears, which are associated with severe and extreme turbulence affecting aircraft takeoff



217 and landing. Furthermore, this capability provides valuable warnings for aircraft
218 operations at Nakawa Airport.

219 The atmosphere above and surrounding the mountainous terrain is
220 characterized by three distinct regions or inclined layers, comprising the thermal
221 structure undergoing diurnal variations and forming diurnal winds: slope
222 atmosphere, valley atmosphere, and mountain atmosphere(Zardi, D.2013). It is
223 challenging to observe any pure form of diurnal mountain wind system, as each
224 component interacts with the others. Well-organized thermally driven flows can be
225 identified over a broad spatial scale, ranging from the dimensions of the largest
226 mountain ranges to the smallest local topography. Therefore, concerning wind shear
227 in mountainous and foothill areas, wind shear in mountainous areas tends to be
228 smaller. When airflow passes through mountain ridges, the lower-level airflow
229 experiences significant compression. According to the conservation of flux, the
230 acceleration effect on lower-level airflow exceeds that on upper-level airflow,
231 resulting in an overall reduction in wind shear. When the acceleration effect on
232 lower-level airflow is significant while the upper-level acceleration effect is weak or
233 absent, negative wind shear occurs. Overall, the intensity of low-level wind shear
234 may be greater near mountain foothills or ridges and lesser in valleys or slopes.
235 Hence, the regions of maximum wind shear simulated by CALMET near mountain
236 foothills or ridges are more consistent with reality than those by WRF.



237

238 Figure 3: Vertical Wind Shear (VWS) at 16:00 on July 3, 2022, simulated by
239 CALMET (a) and WRF (b) (Unit: m/s/10m). Triangles indicate the locations of
240 maximum values.

241 Figure 4 presents the time series of maximum VWS simulated by WRF and
242 CALMET. It can be observed that both WRF and CALMET simulations exhibit a clear
243 diurnal pattern in maximum VWS: maximum values are relatively small around
244 dawn and in the morning (1:00 to 12:00), with minimal fluctuations, while they
245 increase significantly in the afternoon and evening (13:00 to 24:00), showing larger



246 variations. However, the maximum values simulated by WRF are generally lower
247 than those by CALMET, with this difference being more pronounced in the afternoon
248 and evening. On July 3rd and 4th, during periods of intense convective activity,
249 CALMET is able to simulate larger fluctuations in maximum VWS compared to
250 normal conditions.

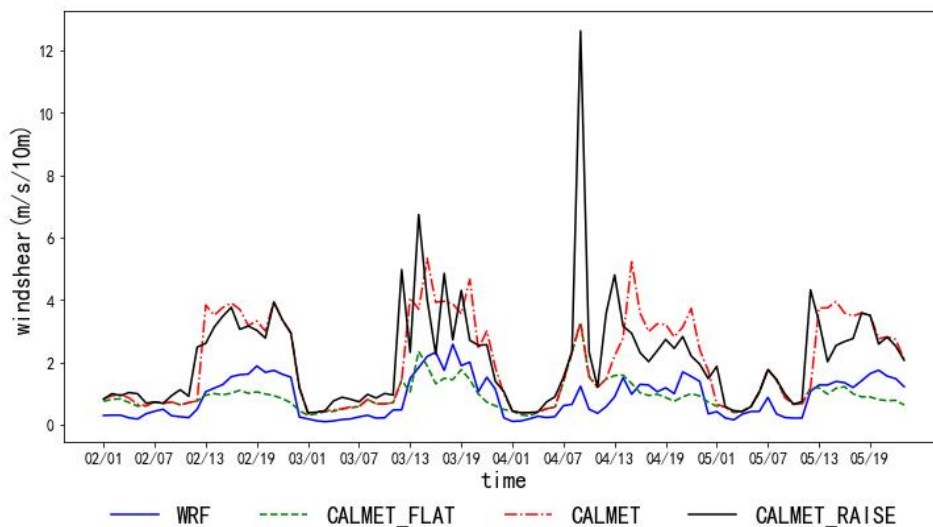
251 In summary, utilizing CALMET for downscaling WRF output of wind fields
252 provides higher resolution and more precise surface conditions, which are
253 advantageous for simulating mesoscale wind shear. This is primarily manifested in
254 the following aspects: the distribution of VWS in the mid-to-low levels is more
255 significantly influenced by terrain, and VWS decreases more rapidly with increasing
256 altitude; the diurnal variation of maximum VWS within VWS regions follows a clear
257 pattern and can reflect the characteristics of intense convection.

258 4.2 Impact of Topography on Wind Shear Simulation

259 Through different terrain configurations, we explored CALMET's detailed
260 terrain impact on low-level wind shear. We found that valley winds affect VWS
261 diurnal variation. Terrain, blocking effects, and slope flow kinematics enhance near-
262 surface airflow diversion, deflection, and ascent over complex terrain, significantly
263 influencing VWS, with the impact decreasing with height.

264 In the CALMET_FLAT experiment, the increase in maximum VWS during the
265 afternoon and evening is minimal (Figure 4), with slight fluctuations and values
266 around 2 m/s/10m, sometimes even lower than WRF. However, good agreement is
267 observed among the three experiments during the early morning and morning
268 periods. In CALMET_RAISE, particularly on July 3rd and 4th during intense
269 convective development, fluctuations in the afternoon and evening are more
270 pronounced compared to CALMET. However, CALMET_RAISE shows stability
271 similar to CALMET just before convective development on July 2nd, except for an
272 unusually high value at 09:00 on July 4th, where fluctuations are more pronounced,
273 but numerically close to CALMET.

274 In the afternoon and evening, CALMET_FLAT shows a significant decrease in
275 maximum VWS, while CALMET_RAISE exhibits more pronounced fluctuations. For
276 example, at 19:00 on July 3rd (Figure 5(a)-(c)), in the CALMET experiment, the
277 maximum VWS (3.56 m/s/10m) occurs in the southeastern foothills and valley
278 areas. In CALMET_FLAT, except for the absence of a high-value area in the southeast,
279 the distribution is similar to CALMET, with a maximum value of 1.77 m/s/10m in
280 the central region, which is also a flat valley area in CALMET. In CALMET_RAISE, due
281 to a sudden 1.5-fold increase in terrain elevation above 2050m, the steep terrain
282 causes chaotic wind shear distribution, with scattered high values in the central
283 region, and the maximum value increases to 4.31 m/s/10m. In summary,
284 transitioning from complex to flat terrain shifts the location of maximum VWS from
285 mountainous areas to flat valleys.



286

287

288

Figure 4: Time series of 10m-30m maximum VWS values of different simulation experiments in the study area

289

290

291

292

293

294

295

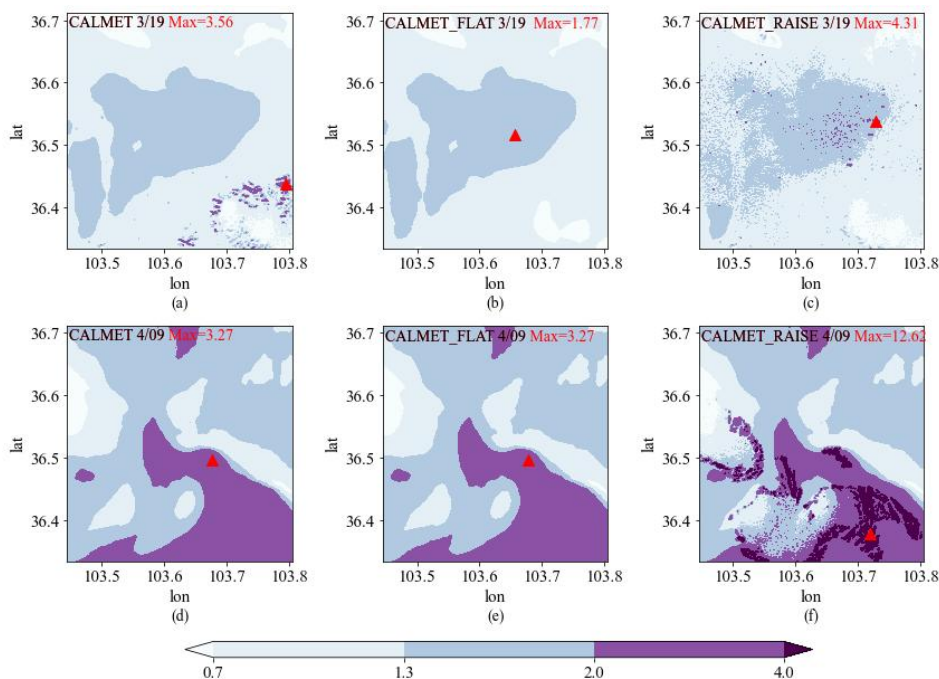
296

297

298

299

This phenomenon is a typical result of valley winds, driven by the interaction between terrain and solar radiation. During the day, sunlight heats the surface, leading to differential heating rates between slopes and valleys due to their distinct topographies. Slopes, receiving direct sunlight, warm up faster than valleys. At night, the surface loses heat, particularly in valleys with good heat dissipation, resulting in strong nighttime cooling effects. The temperature difference between slopes and valleys during the day induces upslope airflow along the slopes. As the heated air ascends, airflow forms over the valleys, as depicted in Figure 5(a) where maximum VWS occurs near mountainous areas. At night, cold air flows downhill along the slopes, forming downslope winds, which reverse the airflow pattern observed during the day.



300

301 Figure 5: VWS distribution of 10m-30m.(a)-(c): 19:00 on July 3, 2022; (d)-(f):
 302 09:00 on 4 July 2022; (a),(d):CALMET; (b),(e):CALMET_FLAT; (c),(f):CALMET_RAISE.

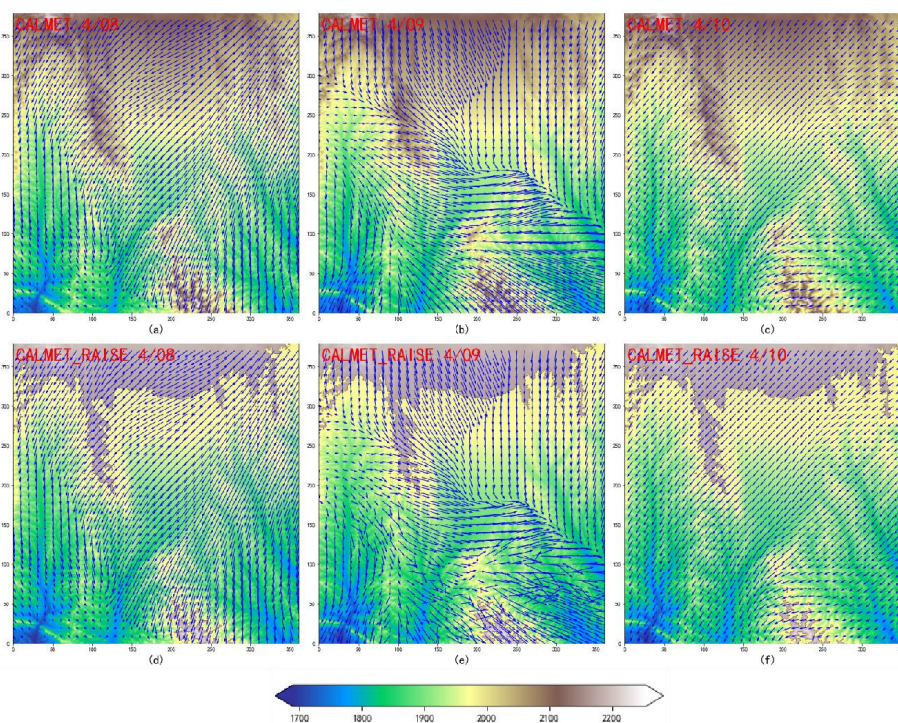
303 The results indicate that CALMET model simulations of VWS are highly
 304 sensitive to terrain: VWS values are generally lower in flat terrain compared to
 305 complex terrain, and the influence of terrain on wind shear diminishes rapidly with
 306 height. In extremely steep terrain, near-surface distribution appears chaotic, but
 307 VWS values notably increase above the surface compared to complex terrain. Across
 308 the three experiments, the absolute differences in VWS decrease with height,
 309 suggesting a diminishing impact of terrain on CALMET model simulations of VWS
 310 with increasing altitude.

311 To investigate extreme high values of VWS in the CALMET_RAISE experiment at
 312 09:00 on July 4th, Figures 5(d)-(f) display the VWS distribution for all experiments
 313 at this time, while Figure 6 presents wind vector maps for three hours for both
 314 CALEMT and CALEMT_RAISE. The VWS distribution for CALEMT and CALEMT_FLAT
 315 is similar, with a peak of 3.27m/s/10m in the central region. Compared to July 3rd
 316 at 19:00, both experiments show extensive high-value areas in the southeast, with
 317 CALMET_RAISE reaching an exceptional maximum of 12.62m/s/10m in the
 318 southeastern valley area. Additionally, CALMET_RAISE exhibits large areas of
 319 exceptionally high values compared to the other experiments.

320 In Figure 6, at 08:00 and 10:00 on July 4th, the prevailing wind direction in the
 321 area is northeast. Both CALMET and CALEMT_RAISE show similar wind field



322 structures, transitioning from northeast to north as terrain slopes southward. When
323 airflow passes through the southern valley, mountain ranges create denser wind
324 vectors and increased speeds. However, at 09:00, a strong northwest airflow
325 converges with the northern airflow, forming a distinct "micro-front." The terrain
326 blocking induces diversion, deflection, and upward motion of the northwesterly
327 wind, creating extensive high-value VWS areas in the southeast. Compared to
328 CALMET, CALEMT_RAISE exhibits a more chaotic wind field due to increased terrain.



329
330
331
332

figure 6. Topographic Elevation (unit: m) and Wind Vector Distribution. (a)-(c)
CALMET; (d)-(f) CALMET_RAISE; (a), (d) July 4th, 08:00; (b), (e) July 4th, 09:00; (c),
(f) July 4th, 10:00.

333 In conclusion, the widespread high-value VWS area observed at 09:00 on July
334 4th resulted from a shift in wind direction to the northwest, encountering minimal
335 velocity reduction before reaching the tall terrain in the south, where the
336 mountainous obstruction led to diversion, deflection, and upward motion. The
337 anomalously high values in the CALEMT_RAISE experiment were attributed to the
338 elevation of the terrain, significantly intensifying the effects of diversion, deflection,
339 and upward motion. This suggests that terrain has a more pronounced impact on
340 CALMET-simulated wind shear during high wind speeds, while its influence is less
341 evident during low wind speeds. Therefore, heightened awareness of low-level wind
342 shear occurrence is warranted in complex terrain.



343 **4 Conclusion**

344 In order to investigate whether higher-resolution numerical models yield
345 better simulation results for low-level wind shear, this study focuses on a severe
346 convective weather event that occurred in the vicinity of Zhongchuan Airport on
347 July 2, 2022. The WRF/CALEMT coupled model is utilized to simulate the wind field,
348 and the influence of terrain variations on CALMET-simulated wind shear is explored.
349 The main conclusions are as follows:

350 (1) CALMET improves the simulation of near-surface winds, bringing them
351 closer to observed data than WRF, thereby facilitating more accurate modeling of
352 low-level wind shear.

353 (2) The diurnal variation of VWS shows a distinct pattern. CALMET exhibits
354 higher VWS compared to WRF, especially during the afternoon and evening. During
355 periods of intense convective activity, CALMET captures larger VWS fluctuations,
356 including higher peak values. CALMET's finer terrain features result in a VWS
357 distribution that better aligns with terrain effects, with VWS generally higher near
358 foothill areas compared to mountains, and a more pronounced decrease with
359 altitude.

360 (3) Terrain sensitivity experiments show that during early morning and
361 morning hours, the maximum VWS of the three experiments were similar, occurring
362 in flat regions with minimal terrain influence. However, in the afternoon and
363 evening, CALMET_FLAT shows decreased maximum VWS values, while
364 CALMET_RAISE exhibits drastic fluctuations, with peak values near mountainous
365 areas, indicating significant terrain influence. Moreover, the impact of terrain on
366 CALMET-simulated VWS diminishes with altitude. These findings highlight the
367 substantial influence of terrain on CALMET, particularly during periods of high wind
368 speeds.

369 (4) The occurrence of abnormally high VWS values in the simulations is
370 attributed to strong disturbances caused by tall terrain features: wind direction
371 shifts to northwest winds, encountering minimal reduction in wind speed before
372 encountering the tall terrain in the southern region. CALMET_RAISE elevates the
373 terrain from its original level, enhancing channeling, swirling, and updraft effects.

374 The research findings of this study are solely based on a short-term simulation
375 period of weather events in the Zhongchuan Airport area. Our future work will
376 expand to include longer simulation periods in more airports and regions with
377 complex terrain. This expansion aims to examine and quantify the additional value
378 provided by CALMET in simulating low-level wind shear.

379

380 *Competing Interests.* The corresponding author declares that all authors have no
381 competing interests.



382 **Acknowledgment**

383 This work was supported by the Joint Funds of the National Natural Science
384 Foundation of China (Grant No. U2342205), the Gansu Provincial Association of
385 Science and Technology Innovation Drive Promotion Project (Grant No.
386 GXH20230817-7), and the Key Natural Science Foundation of Gansu Province (Grant
387 No. 23JRRA1030). We extend our sincere appreciation to the funding agencies for
388 their support.

389 Additionally, we would like to express our gratitude to the Supercomputing
390 Center of Lanzhou University for their assistance.

391

392 **References**

393 [1]Evans J, Turnbull D. Development of an automated windshear detection system
394 using Doppler weather radar[J]. Proceedings of the IEEE, 1989, 77(11): 1661-1673.

395 [2] Fujita T T, Caracena F. An analysis of three weather-related aircraft accidents[J].
396 Bulletin of the American Meteorological Society, 1977, 58(11): 1164-1181.

397 [3]Colman B, Cook K, Snyder B J. Numerical weather prediction and weather
398 forecasting in complex terrain[M]//Mountain Weather Research and Forecasting:
399 Recent Progress and Current Challenges. Dordrecht: Springer Netherlands, 2012:
400 655-692.

401 [4]Hon K K. Predicting low-level wind shear using 200-m-resolution NWP at the
402 Hong Kong International Airport[J]. Journal of Applied Meteorology and Climatology,
403 2020, 59(2): 193-206.

404 [5]Chan PW, Hon KK (2016b) Observation and numerical simulation of terrain-
405 Induced windshear at the Hong Kong International Airport in a planetary boundary
406 layer without temperature inversions. Adv Meteorol Artic ID. [https:// doi.
407 org/10.1155/2016/1454513](https://doi.org/10.1155/2016/1454513)

408 [6]Chen F, Peng H, Chan P, et al. Identification and analysis of terrain-induced low-
409 level windshear at Hong Kong International Airport based on WRF-LES combining
410 method[J]. Meteorology and Atmospheric Physics, 2022, 134(4): 60.

411 [7]Li L, Shao A, Zhang K, et al. Low-level wind shear characteristics and lidar-based
412 alerting at lanzhou zhongchuan international airport, China[J]. Journal of
413 Meteorological Research, 2020, 34(3): 633-645.

414 [8]Dang, B., W. Z. Sun, J. Y. Wang, et al., 2013: Analysis of low-altitude wind shear
415 cases at Lanzhou Zhongchuan Airport during 2004–2007. J. Lanzhou Univ. (Nat. Sci.),
416 49, 63–69, doi:



- 417 10.3969/j.issn.0455-2059.2013.01.012. (in Chinese)
- 418 [9] Jiang Lihui, Liu Xiaoyu, Li Zhen, et al. Study on the influence of terrain and
419 buildings around Lanzhou Zhongchuan Airport on wind field [J]. Computer and
420 Digital Engineering, 2018, 46(3): 561-565,626.
- 421 [10]Zhang D, Chen L, Zhang F, et al. Numerical simulation of near-surface wind
422 during a severe wind event in a complex terrain by multisource data assimilation
423 and dynamic downscaling[J]. Advances in Meteorology, 2020, 2020: 1-14.
- 424 [11]Liao R, Fang X, Liu H, et al. Wind characteristic in the complex underlying
425 terrain as studied with CALMET system[C]//Journal of Physics: Conference Series.
426 IOP Publishing, 2021, 2006(1): 012053.
- 427 [12]Tang S, Huang S, Yu H, et al. Impact of horizontal resolution in CALMET on
428 simulated near-surface wind fields over complex terrain during Super Typhoon
429 Meranti (2016)[J]. Atmospheric Research, 2021, 247: 105223.
- 430 [13]Scire J S, Robe F R, Fernau M E, et al. A user's guide for the CALMET
431 Meteorological Model[J]. Earth Tech, USA, 2000, 37.
- 432 [14]Bretschneider, L.; Hankers, R.; Schönhals, S.; Heimann, J.-M.; Lampert, A. Wind
433 Shear of Low-Level Jets and Their Influence on Manned and Unmanned Fixed-Wing
434 Aircraft during Landing Approach. *Atmosphere* **2022**, *13*, 35.
435 <https://doi.org/10.3390/atmos13010035>
- 436 [15]Keohan, C. Ground-based wind shear detection systems have become vital to
437 safe operations. *ICAO J.* **2007**, *62*, 16–19, 33–34.
- 438 [16]Eggers, A.J., Jr.; Digumarthi, R.; Chaney, K. Wind Shear and Turbulence Effects on
439 Rotor Fatigue and Load Control. *J. Sol. Energy Eng.* **2003**, *125*, 402–409.
- 440 [17]Roland, J. White Effect of wind shear on airspeed during airplane landing
441 approach. *J. Aircr.* **1992**, *29*, 237–242.
- 442 [18]Zardi, D., Whiteman, C.D. (2013). Diurnal Mountain Wind Systems. In: Chow, F.,
443 De Wekker, S., Snyder, B. (eds) Mountain Weather Research and Forecasting.
444 Springer Atmospheric Sciences. Springer, Dordrecht. [https://doi.org/10.1007/978-](https://doi.org/10.1007/978-94-007-4098-3_2)
445 [94-007-4098-3_2](https://doi.org/10.1007/978-94-007-4098-3_2)